Chinese Chemical Letters 34 (2023) 107392

Contents lists available at ScienceDirect

Chinese Chemical Letters

journal homepage: www.elsevier.com/locate/cclet

Porous 2D CuO nanosheets for efficient triethylamine detection at low temperature

Feng Wang[a,1], Haoran Zhong[a,1], Zhenlu Chen[a], Ding Wang[a,*], Zhuangchai Lai[b], Yonghui Deng[c], Xianying Wang[d]

[a] School of Materials and Chemistry, University of Shanghai for Science & Technology, Shanghai 200093, China
[b] Department of Applied Physics, The Hong Kong Polytechnic University, Hong Kong, China
[c] Department of Chemistry, Fudan University, Shanghai 200433, China
[d] Shanghai Institute of Ceramics, Chinese Academy of Sciences, Shanghai 200050, China

ARTICLE INFO

Article history:
Received 18 December 2021
Revised 23 February 2022
Accepted 30 March 2022
Available online 4 April 2022

Keywords:
CuO nanosheets
Gas sensor
Porous materials
Triethylamine detection
Low operating temperature

ABSTRACT

The freshness of seafood can be judged by detecting the concentration of triethylamine (TEA). In this work, 2D CuO porous nanosheets (CuO PNs) were prepared by a graphene oxide template method and their particle sizes were regulated by changing the calcination temperature. Their structure, morphology and gas sensing performances were investigated by various characterization methods. The response (R_g/R_a) of the gas sensor based on CuO PNs calcined at 700 °C was as high as 440-100 ppm TEA at the operating temperature of 40 °C. The detection limit was as low as 0.25 ppm. In addition, the gas sensor has good selectivity and stability. The excellent TEA sensitivity is mainly resulted from the appropriate particle size and loose porous framework. This work not only paves the way to explore the novel low temperature TEA gas sensors, but also provides deep insight on improving the structure and properties of gas sensitive materials by controlling the calcination temperature.

As one of the most commonly used organic bases, triethylamine (TEA) is widely used in pesticides (glyphosate), medicine as intermediates. Due to toxicity and irritation, concentrations of TEA above 10 ppm in the air can affect human health and even cause death in serious cases [1]. In addition, since seafood products would release organic amine when decaying, the freshness of seafood can be judged based on the measured concentration of TEA. Moreover, the mixture of TEA vapor and air is highly explosive when exposed to flame. Therefore, precise detection of TEA gas is of great significance. Although the traditional detection methods such as colorimetry and chromatography are effective in the detection of TEA, they also suffer from the complicated detection process and expensive detection equipment, restricting the further practical application. Compared with these methods, the gas sensor with faster response, smaller volume and convenient carrying would be a better alternative.

To date, metal oxide semiconductor (MOS) based gas sensor has been widely used in TEA detection due to their low price, high sensitivity and ease of integration [2–5]. For example, Xue *et al.* synthesized flower-like CeO_2-SnO_2 composites by the one-step hydrothermal reaction and their response was 252.2 ppm toward 200 ppm TEA at 310 °C [6]. Zou *et al.* prepared hollow SnO_2 microfiber through biomass conversion strategy, which delivered a response of 49.5 ppm to 100 ppm TEA at 270 °C [7]. Zhai *et al.* reported three-dimensional WO_3 hollow microspheres, showing a response of 16 ppm to 50 ppm TEA at 220 °C [8]. Li *et al.* synthesized PdPt/a-Fe_2O_3, which obtained a response of 98 ppm to 50 ppm TEA at 190 °C [9]. However, although MOS sensors can be used for TEA detection, most sensors still suffer from problems such as high operating temperature and low sensitivity.

As one of the most promising candidates for gas sensor, p-type MOS sensitive materials usually have good gas selectivity and low operating temperature [10–12]. As a p-type semiconductor with small band gap, CuO has a wide application prospect in the fields of sensors, catalysts, superconductors, supercapacitors and so on [13–15]. Until now, various excellent methods for preparing CuO nanostructures with different morphology have been well established, including nanosheets, nanofibers, nanospheres, nanowires, *etc.* [16–19]. Among them, the two-dimensional structure has significant advantages in the field of gas sensitivity due to its large specific surface area and abundant active sites. To further enhance the gas sensing performance, structural design has been widely adopted [20–24]. It has been found that grain size, porosity and

* Corresponding author.
E-mail address: wangding@usst.edu.cn (D. Wang).
[1] These authors contributed equally to this work.

https://doi.org/10.1016/j.cclet.2022.03.115
1001-8417/

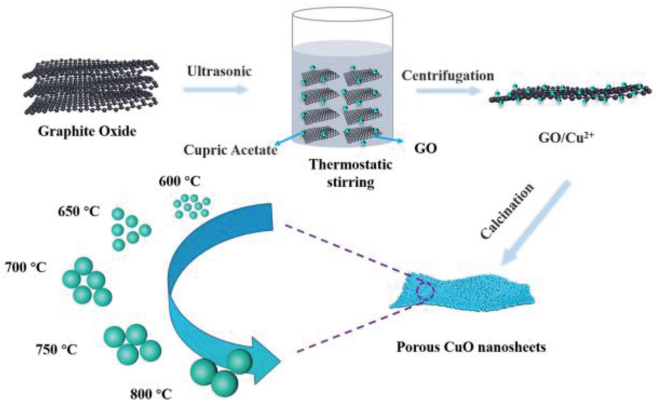

Fig. 1. Schematic illustration for fabrication of 2D CuO PNs by GO templated process.

specific surface area of the material have great impacts on the heat treatment of the precursor [25–27]. For example, NiO nanosheets with different pore sizes and grain sizes were obtained by changing the calcination temperature, exhibiting improved gas sensing properties [25]. As another example, Wu *et al.* obtained CuO with different morphologies by controlling the calcination condition and evaluated its effect on the gas sensing performance of the samples [28]. Therefore, systematical study of the heat treatment effects on the morphology, crystallinity and porosity of CuO is highly desirable, which is of great significance for improving the performance of gas sensing.

Herein, we report a facile method to prepare a series of 2D CuO porous nanosheets (PNs) for the high-efficiency TEA detection. The CuO nanosheets were first synthesized by using graphene oxide (GO) as template, which were then calcined at different temperatures to form the desired CuO PNs. The morphology, structure and elemental composition of the materials were fully characterized. With TEA as target detection gas, the optimum operating temperature, selectivity, response and stability of CuO were investigated by a gas sensor evaluation system. Finally, the gas sensing mechanism was discussed.

The detailed process for the preparation of CuO PNs was shown in Fig. 1 and Supporting information. The schematic illustration indicated that cupric ion is firmly attached to the GO surface under the action of electrostatic force. The functional groups on the GO surface make the GO surface negatively charged. Then, the CuO PNs with different grain sizes were obtained after heat treatment at different temperature.

The morphology of CuO PNs was characterized by scanning electron microscope (SEM) and transmission electron microscope (TEM). As shown in Figs. 2a-e, all the CuO PNs calcined at 600-800 °C consisted of in-plane mesopores with interconnected framework. The TEM images of CuO PNs samples in Figs. 2f-j also proved the 2D porous nanosheets morphologies. In addition, the particle distribution of samples calcined at different temperatures was calculated, showing average particle sizes (insets of Figs. 2f-j) of 30 nm, 39 nm, 46 nm, 58 nm, 140 nm for CuO-600, CuO-650, CuO-700, CuO-750, CuO-800, respectively. Obviously, the particle sizes increased with the increasing of calcining temperature.

In order to understand the material morphology evolution under different calcination temperature, TG-DSC was performed to investigate the thermal behavior of the GO/cupric acetate precursor. As shown in Fig. 2k, a total weight loss of 67 wt% was observed during thermogravimetric test, which is mainly distributed in the following three temperature ranges. The first stage (~10 wt% weight loss) below 200 °C corresponded to the desorption of adsorbed water. The second weight loss stage (~27 wt%) during the temperature range of 200-400 °C might be related to the decomposition of cupric acetate and functional groups on GO. The third stage (~30 wt% weight loss) at around 400 °C was the combustion of GO. Furthermore, no obvious weight loss was observed above 400 °C indicated the complete removal of GO. Therefore, we can eliminate the interference of GO by calcination above 600 °C.

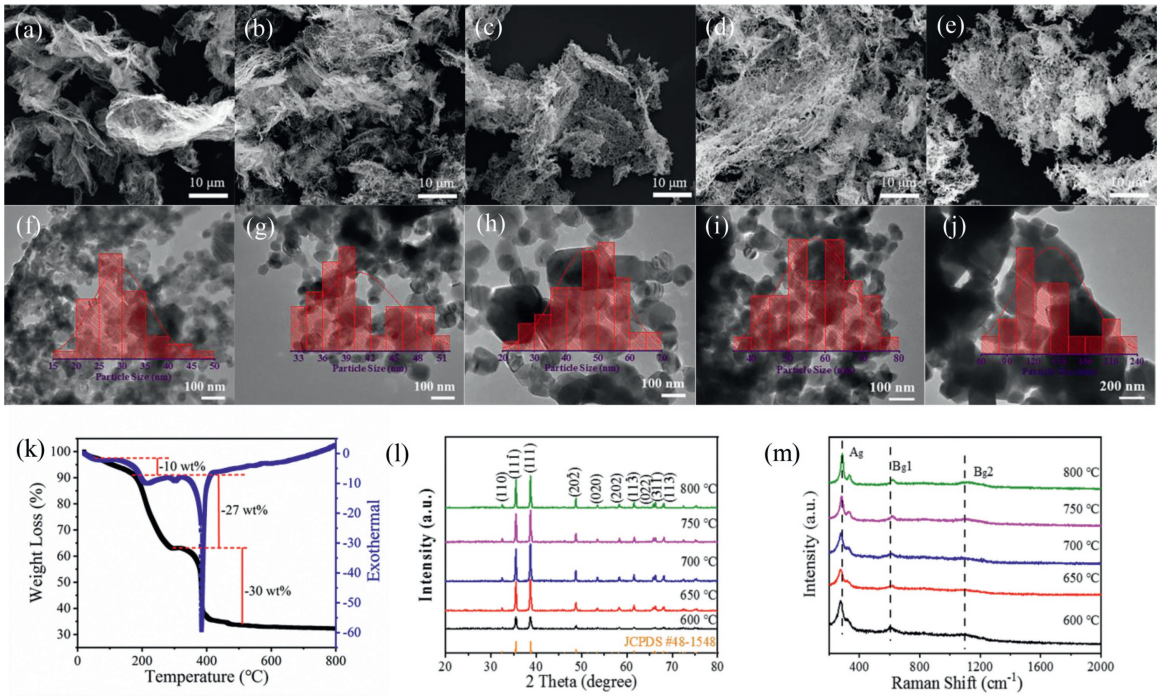

Fig. 2. SEM images of (a) CuO-600, (b) CuO-650, (c) CuO-700, (d) CuO-750, (e) CuO-800. TEM images of (f) CuO-600, (g) CuO-650, (h) CuO-700, (i) CuO-750, (j) CuO-800. The insets are the size distribution of CuO calcined at different temperature. (k) TGA analysis of the precursor annealed in air. (l) XRD patterns of CuO products calcined at different temperatures. (m) Raman spectra of CuO products calcined at different temperatures.

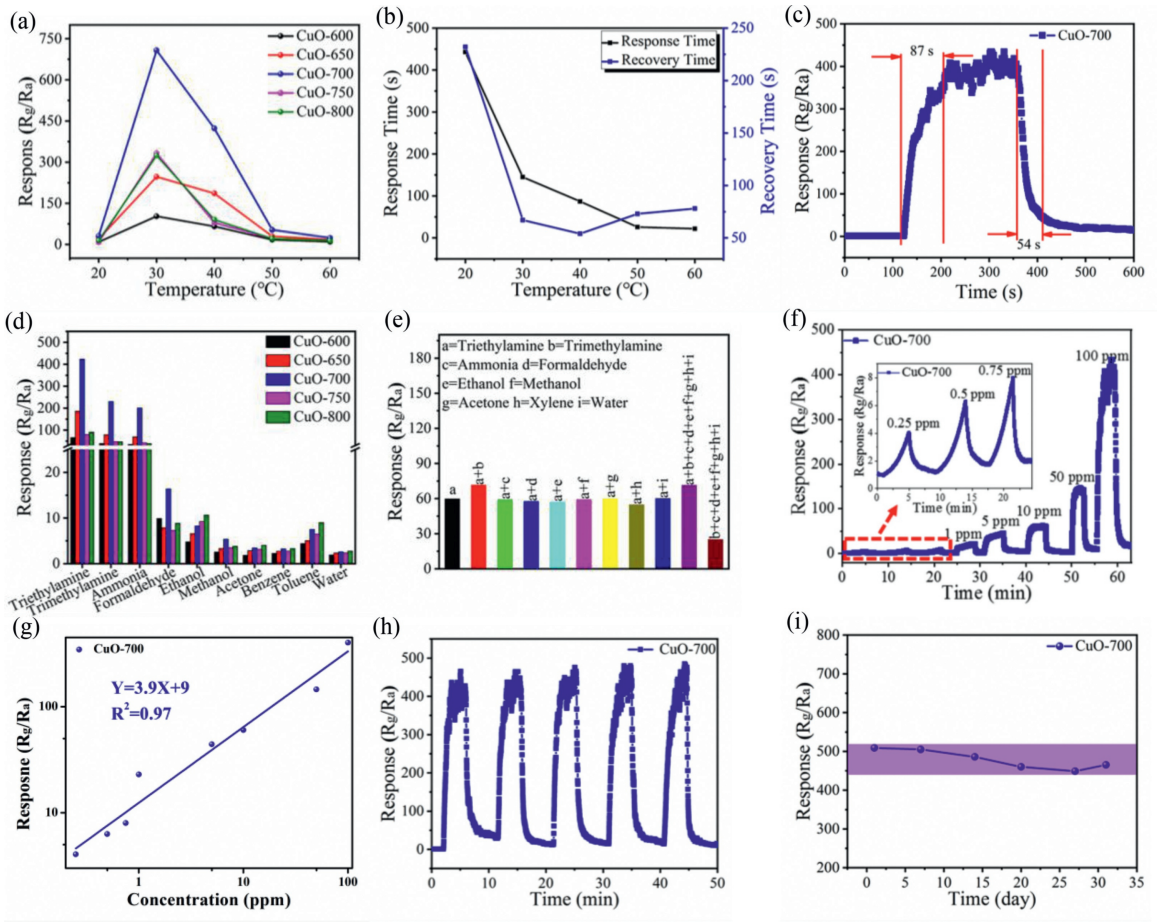

Fig. 3. (a) Response of sensors *versus* operating temperature to 100 ppm TEA. (b) The operating temperature *vs.* response/recovery time of the sensor (CuO-700). (c) Response curve of CuO-700 sensor to 100 ppm TEA. (d) Response of the sensor to 100 ppm different gases at 40 °C. (e) Responses of CuO-700 sensor to mixture vapors at 40 °C. (f) Response/recovery curves of the sensor to 0.25-100 ppm TEA (The inset is response/recovery curves of sensors to 0.25-1 ppm TEA.). (g) The relationship between response and concentration of the sensor. (h) 5 circles of the response to 100 ppm TEA based on CuO-700 at 40 °C. (i) Long-term stability of the sensor to 100 ppm TEA at 40 °C.

As shown in Fig. S2a (Supporting information), the corresponding isotherm curves for CuO-700 exhibited a typical IV isotherm with a H_3 hysteresis loop in the relative pressure (P/P_0) range of 0.1-1, which suggested the presence of the mesoporous.

XRD patterns of CuO PNs calcined at the temperature range between 600 and 800 °C were displayed in Fig. 2l. All diffraction peaks matched well with those of standard XRD patterns of CuO (JCPDF No. 48-1548) [29]. No phases that correspond to impurities were observed in the patterns. As the calcination temperature increasing, the crystallinity of the sample become higher and large crystals could be formed, which was confirmed by the trend that the diffraction peak in the XRD pattern becomes stronger and sharper. According to Scherrer's formula, the average grain sizes of CuO at different calcination temperatures (600-800 °C) are 25.9 nm, 34.2 nm, 50.4 nm, 52.2 nm and 57.2 nm, respectively. The variation trend of particle size was consistent with results shown in TEM.

Raman spectra of CuO PNs calcined at the temperature between 600 °C and 800 °C were shown in Fig. 2m. The scattering bands corresponded to the A_g, B_g1 and B_g2 vibrational modes of CuO observed at the wavenumbers of 276-286 cm^{-1}, 323-333 cm^{-1}, and 608-618 cm^{-1}, respectively. With the increase of calcination temperature, the Raman peaks became stronger and sharper, and shift to higher wavenumber, which was attributed to the increasing of the grain size. Due to the size effect, the increase of CuO grain size leads to the narrowing of Raman peak and the blue shift of peak position [30]. GO was completely removed from the CuO PNs based on the absence of carbon characteristic peaks in the Raman spectra (Fig. 2m).

The chemical states of the sample were studied by X-ray photoelectron spectroscopy (XPS). The full survey XPS spectrum of CuO-700 was shown in Fig. S1a (Supporting information), suggesting the coexistence of Cu, O and C elements. As shown the high-resolution spectrum of Cu 2p for CuO-700 (Fig. S1b), the characteristic peaks at 934 eV and 954 eV are corresponded to Cu $2p_{3/2}$ and $2p_{1/2}$, respectively. Besides, the peaks at 941.5 eV, 944.4 eV and 962.7 eV can be assigned to the shake-up satellite of Cu $2p_{3/2}$ and $2p_{1/2}$, which are the characteristic peaks in the XPS spectrum of CuO [31,32]. Thus, the copper in CuO-700 mostly exists in the oxidation state.

Sensing properties of CuO PNs calcined at different temperatures were measured through a gas sensor evaluation system. The optimal operation temperature was obtained by testing the sensors from 20 °C to 60 °C. As shown in Fig. 3a, the response values (R_g/R_a) of the sensors to 100 ppm TEA increased as the temperature increasing from 20 °C to 30 °C and decreased as the temperature increasing from 30 °C to 60 °C. The maximum response values were obtained at 30 °C. The optimum calcination temperature of the precursor was 700 °C as the maximum response value was obtained. It is noteworthy that a maximum sensitivity of ~750-100 ppm TEA at 30 °C can be achieved on the CuO-700 sensor. Fig. 3b showed the relationships between operating temperature and response/recovery times of CuO-700 sensor. Although the CuO-700 sensor has the highest sensitivity to 100 ppm TEA at 30 °C, the

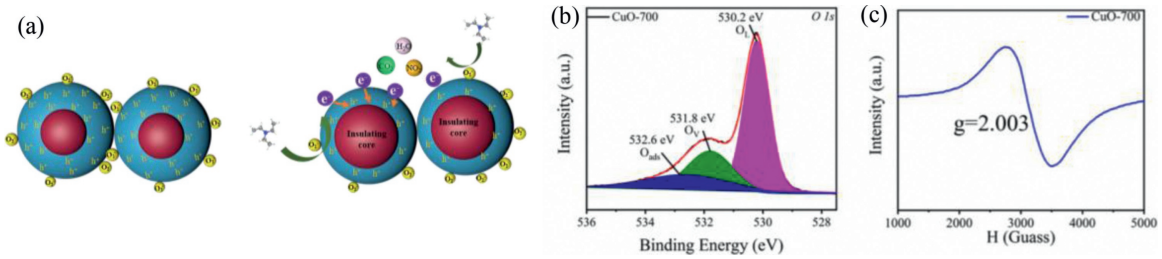

Fig. 4. (a) Schematic diagram of TEA sensing mechanism. (b) The high-resolution spectra of O 1s for CuO calcined at 700 °C. (c) ESR spectra of CuO-700 recorded at 25 °C.

response time was about 150 s, which was too long to be applied in practical application. In contrast, as shown in Fig. 3c, the response/recovery times of the sensor at 40 °C is reduced to 87 s/54 s and the sensitivity remains 440 for 100 ppm TEA. Therefore, considering both the sensitivity and response/recovery performances of the sensor, 40 °C was selected as the optimal operating temperature. The rapid response/recovery rate of CuO PNs to TEA is attributed to its unique porous structure. The porous structure shortens the gas transmission path and improves the response speed. Beyond that, abundant pores also make the gas easier to diffuse and improve the recovery speed. Fig. 3d showed the selectivity of the sensors. All sensors only have high response to TEA, while their response to other interfering gases is relatively low. In order to simulate actual detecting environment, the sensor was exposed to a mixture of TEA and different interfering gases. The concentration of TEA in the mixed gases was maintained at 10 ppm and the operation temperature was kept at 40 °C. Fig. 3e indicated that CuO-700 showed better anti-interference performance in a complicated atmosphere as compared with other samples. Obviously, the response towards interfering vapors was much less than toward pure TEA.

The response/recovery curve of CuO-700 sensor with increasing TEA concentration was shown in Fig. 3f. The sensitivity of CuO-700 sensor increased as the TEA concentration increasing from 0.25 ppm to 100 ppm. In order to reveal the relationship between response and gas concentration, the correlation line of the sensor in Fig. 3g is fitted. The response value has an approximate linear relationship with the gas concentration in the double logarithmic coordinate, indicating its great potential for practical detection of TEA. The limit of detection (LOD) of CuO-700 was as low as 0.25 ppm, implying its application for indoor TEA detection with the test requirement of 10 ppm. Excellent repeatability is the premise for the application of gas sensor in practice. As shown in Fig. 3h, the sensitivity of CuO-700 showed negligible change in the five cycles test. Moreover, there is no obvious change in the response/recovery curve measured from the sensors, proving its good stability and repeatability. The long-term stability of CuO-700 was studied by testing the sensor every 5 days within a month. As shown in Fig. 3i, the response value of the sensors showed little fluctuation as compared with the original value during the one-month test.

The gas sensing properties of CuO PNs sensor to TEA are compared with other gas sensors in Table S1 (Supporting information) [6-8,28,33-36]. In contrast to most of the TEA gas sensors, CuO PNs gas sensor in this work had a relatively lower operation temperature close to the room temperature, low LOD and extremely high sensitivity. Generally, the operating temperature of TEA gas sensors is higher than 100 °C, while the optimal operating temperature of the porous CuO nanosheets gas sensor obtained was only 40 °C. The response of the porous CuO nanosheets gas sensor to 100 ppm TEA was higher (440) than most of the previously reported results. The outstanding sensing performance was attributed to the unique framework structure and suitable particle size of CuO PNs. Response of CuO-700 to 100 ppm of TEA under different relative humidity (RH%) were also tested. As shown in Fig. S3 (Supporting information), the response values decreased with the increase of the humidity from 40 RH% to 70 RH%. The OH group of H_2O may occupy the adsorption site and react with TEA by competing with surface oxygen. This may be the reason for the decline of gas sensing performance of materials in humid environment.

As shown in Fig. 4a, when oxygen molecules adsorbed on the surface of CuO PNs and accepted electrons to form oxygen ions (O_2^-, O^-, or O^{2-}) in air, the hole accumulation layer (HAL) was formed and resulted in the decrease of the resistance of CuO. Then, when the sensor was exposed in TEA vapor, a virtual reaction occurred between adsorbed oxygen species and TEA molecules. In this case, a few holes were consumed and led to the increase of the resistance of CuO [37]. The adsorbed oxygen species varied at different operating temperature (top) [38]. In this work, all gas sensitivity tests are carried out at 40 °C. Therefore, the adsorbed oxygen species can be described as following:

$$O_2\ (gas) \rightarrow O_2\ (ads) \quad (1)$$

$$O_2\ (ads) + e^- \rightarrow O_2^-\ (ads)\ (top < 100\ °C) \quad (2)$$

The reaction between TEA and adsorbed oxygen species can be described with the following equation [39]:

$$4N(C_2H_5)_3 + 43O_2^- \rightarrow 24CO_2 + 4NO_2 + 30H_2O + 43e^- \quad (3)$$

The excellent sensing properties of the CuO PNs sensor were attributed to the porous nanostructure including suitable particle size and abundant in-plane mesopores. First, the CuO-700 prepared by GO template method had a porous structure, greatly reducing the transport path and effectively improved the gas sensing response. In addition, the abundant mesopores increase the specific surface area and active sites of the material, which is conducive to the adsorption of gas molecules on the material surface, and then improve the response to TEA. Second, the grain size of the materials also has a significant effect on the gas sensing performance. If the grain size is less than two times of the Debye length of the material, the grains on the surface of the material will be in the depletion region, and the conductivity of the material is controlled by the grains [40,41]. With the rise of the calcination temperature, the grain size of CuO increased gradually. The Debye length of CuO was reported to 23 nm [42]. The average grain sizes of CuO-600, CuO-650, CuO-700, CuO-750, CuO-800 were 30 nm, 39 nm, 46 nm, 58 nm, 140 nm, respectively, indicating that the crystallites of CuO-600, CuO-650 and CuO-700 could be depleted, which may imply that most CuO nanoparticles were active and provided abundant active sites for oxygen species and TEA gas molecules. Fig. 4b and Figs. S1c-f (Supporting informaiton) showed the high-resolution XPS spectrum of O 1s for CuO calcined at different temperatures which could be deconvoluted into three peaks at 530.2 eV, 531.8 eV and 532.6 eV, which could be assigned to lattice oxygen (O_L), oxygen vacancy (O_V) and adsorbed oxygen (O_{ads}), respectively. Table S2 showed the relative percentage of O_L, O_V

and O_{ads} peak areas, respectively. The relative percentage of O_{ads} peak area for CuO-700 was the highest among the five samples. It demonstrated that CuO-700 had the highest amounts of adsorbed oxygen, which could enhance the sensing performance of CuO. As shown in Fig. 4c, a strong signal caused by oxygen vacancies can be seen at $g = 2.003$, which indicates that there are a large number of oxygen vacancies on the surface of CuO-700 [43,44]. A large number of oxygen vacancies on the surface of CuO is also one of the reasons why the material has excellent gas sensing properties.

In summary, a high-efficiency sensor for the detection of TEA gas was successfully fabricated based on 2D CuO PNs. The CuO PNs was prepared by GO template method. The CuO sensors exhibited superior TEA sensing performance. CuO prepared by calcining at 700 °C had the highest response value. In addition, the CuO PNs sensor showed good performance with low operating temperature and LOD. These unique sensing properties of CuO PNs sensor were attributed to the porous nanostructure of the material.

Declaration of competing interest

The authors declare that they have no known competing financial interests or personal relationships that could have appeared to influence the work reported in this paper

Acknowledgments

This study was financially supported by the National Natural Science Foundation of China (No. 62071300), Science and Technology Commission of Shanghai Municipality (Nos. YDZX20213100003002, 19ZR1435200, 20490761100), Innovation Program of Shanghai Municipal Education Commission (No. 2019-01-07-00-07-E00015), Program of Shanghai Academic/Technology Research Leader (No. 19XD1422900), Key Basic Research Program of Science and Technology Commission of Shanghai Municipality (No. 20JC1415300), Foshan Science and Technology Innovation Program (No. 2017IT 100121).

Supplementary materials

Supplementary material associated with this article can be found, in the online version, at doi:10.1016/j.cclet.2022.03.115.

References

[1] Y.Y. Shang, W.Q. Shi, R.H. Zhao, et al., Chin. Chem. Lett. 31 (2020) 2055–2058.
[2] J.J. Liu, L.Y. Zhang, J.J. Fan, et al., Sens. Actuator. B 331 (2021) 129425.
[3] Y. Sun, Z. Dong, D. Zhang, et al., Sens. Actuator. B 326 (2021) 128791.
[4] W.J. Wei, J.X. Zhao, S.X. Shi, et al., J. Mater. Chem. C 8 (2020) 6734–6742.
[5] X.L. Xu, S.Y. Wang, W.W. Liu, et al., Sens. Actuator. B 333 (2021) 129616.
[6] D.P. Xue, Y. Wang, J.L. Cao, et al., Nanomaterials-Basel 8 (2018) 1025.
[7] Y.H. Zou, S. Chen, J. Sun, et al., ACS Sens. 2 (2017) 897–902.
[8] C.B. Zhai, M.M. Zhu, L. Jiang, et al., Appl. Surf. Sci. 463 (2019) 1078–1084.
[9] G. Li, Z. Ma, Q. Hu, et al., ACS Appl. Nano Mater. 4 (2021) 10921–10930.
[10] P.F. Cheng, F. Dang, Y.L. Wang, et al., Sens. Actuator. B 328 (2021) 129028.
[11] S.X. Cai, X.Q. Song, Z.T. Chi, et al., Sens. Actuator. B 343 (2021) 130118.
[12] M.T. Vijjapu, S.G. Surya, J.H. He, et al., ACS Appl. Mater. Interfaces 13 (2021) 40460–40470.
[13] K. Rajendran, N. Pandurangan, C.P. Vinod, et al., Appl. Catal. B 297 (2021) 120417.
[14] Y.Q. Guo, X.F. Hong, Y. Wang, et al., Adv. Funct. Mater. 29 (2019) 1809004.
[15] M.G. Zhao, J.T. Yu, X.M. Zhang, et al., Adv. Funct. Mater. 31 (2021) 2008604.
[16] Y. Yang, L.M. Sun, W.W. Zhan, et al., J. Mater. Chem. A 9 (2021) 4310–4316.
[17] H.S. Xie, X.F. Liu, R. Wu, et al., ACS Appl. Energy Mater. 3 (2020) 7325–7334.
[18] P.Y. Wang, L.L. Peng, J.Y. Lin, et al., Chem. Eng. J. 415 (2021) 128901.
[19] H.N. Sun, J.P. Liu, G. Chen, et al., Small Methods (2021) 2101017.
[20] Y.L. Zhang, C.W. Jia, R.N. Tian, et al., Rare Metals 40 (2021) 1578–1587.
[21] J. Hu, X. Chen, Y. Zhang, Sens. Actuator. B 349 (2021) 130738.
[22] X. Chen, J. Hu, P. Chen, et al., Sens. Actuator. B 339 (2021) 129902.
[23] C. Liu, J. Hu, G. Wu, et al., ACS Appl. Mater. Interfaces 13 (2021) 56309–56319.
[24] K. Xu, C.Y. Zhan, W. Zhao, et al., J. Hazard. Mater. 416 (2021) 125906.
[25] N.D. Hoa, C.M. Hung, N.V. Duy, et al., Sens. Actuator. B 273 (2018) 784–793.
[26] Q. Rong, Y. Li, S. Hao, et al., J. Mater. Chem. A 9 (2021) 6529–6537.
[27] K. Zhang, S.W. Qin, P.G. Tang, et al., J. Hazard. Mater. 391 (2020) 122191.
[28] Y.P. Wu, W. Zhou, W.W. Dong, et al., Cryst. Growth Des. 17 (2017) 2158–2165.
[29] W.C. Geng, Z.Y. Ma, Y.J. Zhao, et al., Sens. Actuator. B 325 (2020) 128775.
[30] J.F. Xu, W. Ji, Z.X. Shen, et al., J. Raman Spectr. 30 (1999) 413–415.
[31] X.B. Hu, Z.G. Zhu, Z.H. Li, et al., Sens. Actuator. B 264 (2018) 139–149.
[32] S. Liang, Y.M. Zhou, W.T. Wu, et al., J. Photochem. Photobiol. A 346 (2017) 168–176.
[33] X.N. Meng, M.X. Yao, S.F. Mu, et al., ChemistrySelect 4 (2019) 11268–11274.
[34] H.M. Sun, X.N. Tang, J.R. Zhang, et al., Sens. Actuator. B 346 (2021) 130546.
[35] K. Xu, Q. Tang, W. Zhao, et al., Sens. Actuator. B 302 (2020) 127154.
[36] Q. Wei, J. Sun, P. Song, et al., Sens. Actuator. B 317 (2020) 128205.
[37] S.X. Cao, L.L. Peng, B.T. Liu, et al., J. Alloys Compd. 798 (2019) 478–483.
[38] K.C. Wan, D. Wang, F. Wang, et al., ACS Appl. Mater. Interfaces 11 (2019) 45214–45225.
[39] Y.S. Xu, L.L. Zheng, C. Yang, et al., ACS Appl. Mater. Interfaces 12 (2020) 20704–20713.
[40] X.J. Zhu, X.L. Zhang, X.T. Chang, et al., Sens. Actuator. B 347 (2021) 130599.
[41] M.Z. Jiao, X.Y. Chen, K.X. Hu, et al., Rare Metals 40 (2021) 1515–1527.
[42] Z.Z. Huang, X.M. Wang, F.Z. Sun, et al., Mater. Des. 201 (2021) 109507.
[43] X. An, C. Hu, H. Liu, et al., J. Mater. Chem. A 5 (2017) 24989–24994.
[44] L. Hou, Z. Guan, M. Zhang, et al., Catal. Sci. Technol. 8 (2018) 2809–2817.